Coupled Circuit Numerical Analysis of Eddy Currents in an Open MRI System

Md. Shahadat Hossain Akram[1*], Yasuhiko Terada[1], Ishi Keiichiro[1], Katsumi Kose[1]

[1] *Institute of Applied Physics, University of Tsukuba, Tsukuba, Ibaraki, Japan,*

Short running head: Eddy current analysis of an open MRI system

*Correspondence to:

Md. Shahadat Hossain Akram, Institute of Applied Physics, University of Tsukuba, 1-1-1 Tennoudai, Tsukuba, Ibaraki, Japan 305-8573

Cell-Phone: +81-80-4718-1720

E-mail: sh.arkam@yahoo.com

Keywords: Eddy current, open compact MRI, Eigen method, solid angle, coupled circuit numerical analysis, FID measurements

Abstract

We performed a new coupled circuit numerical simulation of eddy currents in an open compact magnetic resonance imaging (MRI) system. Following the coupled circuit approach, the conducting structures were divided into subdomains along the length (or width) and the thickness, and by implementing coupled circuit concepts we have simulated transient responses of eddy currents for subdomains in different locations. We implemented the Eigen matrix technique to solve the network of coupled differential equations to speed up our simulation program. On the other hand, to compute the coupling relations between the biplanar gradient coil and any other conducting structure, we implemented the solid angle form of Ampere's law. We have also calculated the solid angle for three dimensions to compute inductive couplings in any subdomain of the conducting structures. Details of the temporal and spatial distribution of the eddy currents were then implemented in the secondary magnetic field calculation by the Biot–Savart law. In a desktop computer (Programming platform: Wolfram Mathematica 8.0®, Processor: Intel(R) Core(TM)2 Duo E7500 @ 2.93 GHz 2.93 GHz; OS: Windows 7 Professional; Memory (RAM): 4.00 GB), it took less than three minutes to simulate the entire calculation of eddy currents and fields, and approximately six minutes for X-gradient coil. The results are given in the time–space domain for both the direct and the cross-terms of the eddy current magnetic fields generated by the Z-gradient coil. We have also conducted free induction decay (FID) experiments of eddy fields using a nuclear magnetic resonance (NMR) probe to verify our simulation results. The simulation results were found to be in good agreement with the experimental results. In this study we have also conducted simulations for transient and spatial responses of secondary magnetic field induced by X-gradient coil. Our approach is fast and has much less computational complexity than the conventional electromagnetic numerical simulation methods.

Introduction

Eddy currents are inevitable secondary effects of magnetic resonance imaging (MRI) gradient coils. The switching of the applied signals in the gradient coils generate time- and space dependent magnetic fields that create spatially distributed transient eddy currents in the surrounding conducting structures. Temporal and spatially dependent secondary magnetic fields are generated from these transient eddy currents. These decaying magnetic fields superimposed on the desired gradient field, distort the nuclear magnetic resonance (NMR) localization processes, and create intensity artifacts [1, 2], phase dispersion, imperfect rephasing of echoes, loss of signal, and distortions of images and spectra [3]. For this reason, the implementation of a proper compensation technique in any MRI system requires characterization of the eddy currents.

In this work, we have implemented a new solid angle coupled circuit numerical analysis approach to analyze eddy current responses in open compact MRI systems. The physics behind this method is the multiexponential response of a network of inductively coupled circuits to a time-dependent current signal. This method is very efficient than the traditional electromagnetic simulation approaches in terms of computational complexity, computational time, and as it can handle boundary conditions [4, 5]. Semi-analytic solutions are also possible to get by this method. Conventional methods, such as the finite difference time domain (FDTD) method or the finite element method (FEM), have a time-consuming large-scale computational burden that requires very large memory and a high-performance computer—sometimes with parallel processing environments [6–8]. In addition, because of the large-scale computational complexity that combines the differential and integral techniques, there is a possibility of having numerical artifacts in the final results, like the artifacts because of interpolation in the transformation from lower dimensional grids to higher dimensional grids or field leakage across the boundary because of the slower

propagation in the FDTD grid which differs from the propagation speed in the continuous world and so on [9]. The coupled circuit approach implements the advantages of differential equation and, matrix techniques to solve this system of first order differential equations that make it a mathematically much less complex and faster numerical simulation scheme.

Following the coupled circuit method [10], eddy current conducting structures are modeled as inductively coupled subdomains and simple coupled differential equations are solved to find the transient responses of eddy currents in different subdomains. Studies [10–12] using the coupled circuit approach were done on closed-bore (superconducting magnet) MRI systems and the coupled subdomains assumed for the cylindrical cryogenic walls were of circular ring shaped. Simple inductive coupling formulas for computing the coupling relations between the subdomain and the gradient coils could be implemented in those studies. In references [5, 13] a network simulation - coupled in Fourier space - has been proposed for gradient coils of arbitrary geometry in cylindrical coordinates and validated by simulating the eddy current response in a finite length cylindrical cryostat induced by an actively shielded cylindrical *x*-gradient coil. Recently a Multilayer Integral Method (MIM) has been suggested [4] in which the eddy current conducting surface is approximated to a connected set of discrete mesh of plane triangles. In open MRI systems, the gradient coils are of the planar type, consisting of an upper and a lower coil [14]. Also, the eddy current conducting structures have different geometrical shapes—for example, the local radio frequency (RF) shielding box has a cubic structure [15, 16]. There is no direct traditional formula to compute inductive couplings between a planar gradient coil and different subdomains. As the formulation of a solid angle expression for three dimensions (3D) subtended by a two-dimensional (2D) current-carrying coil of arbitrary shape can be easily performed by simple mathematical manipulations in the Cartesian coordinates [17-21], we have implemented the solid angle form of Ampere's law [22] to compute the inductive coupling between planar

gradient coil and any subdomain. We have calculated the 3D solid angle formula for both Z-gradient (Gz coil) and X-gradient (Gx coil) coil patterns with the aim of computing coupling relations to subdomains in any position. We have also provided details of the solid angle calculation for both Z-gradient and X- or Y-gradient coils. For the calculation of solid angle for Z-gradient coil pattern (circular loop) we have followed the mathematical approaches explained in [17, 19, and 20]. In case of X-gradient coil, because of asymmetric coil position compare to the magnet center, we have followed an efficient segmentation solid angle calculation approach by following the method explained by H. Gotoh, et al [21] in their calculation of solid angle at any field point subtended by a rectangular slit. In our study we have found this approach mathematically less complex, faster in computer simulation, and easier to implement. This segmentation approach can also be possible to implement to calculate solid angle for any type of coil patterns (for example, the area covered in a cylinder by one turn of cylindrical Gx coil can be projected on a plane, and then it is possible to segment that projected area into several rectangular section to calculate the total solid angle subtended by the cylindrical Gx coil). Both the direct and cross-terms of the secondary fields generated by the Z-gradient coil have been simulated in the temporal–spatial domain. We have also conducted free induction decay (FID) measurements of eddy currents by using an NMR probe designed at our laboratory to verify our simulation results. We have found a good agreement between the simulation and the experiment. Simulation of secondary magnetic field responses of X-gradient coil has also been performed and results are given for both transient and spatial response of eddy current fields.

Materials and Methods

A. The Coupled Circuit Method

Because of losses in conducting materials, eddy current responses are characterized as the sum of exponentials with different decay time constants and amplitudes in different conducting structures [3, 23–26]. This multiexponential decay of eddy currents can in turn be modeled by inductive-resistive (*L*–*R*) series circuits comprising conducting structures and current-generating coils [3, 10]. In 1984, Sablik et al. first formulated this concept into a coupled circuit numerical analysis method in which eddy current conducting structures are represented as stacks of inductively coupled subdomains in mutual coupling with the current-generating gradient coils [10]. Further works [5, 11–13] have proven this approach as an efficient, fast, and computationally less complex numerical analysis method than the conventional methods for analyzing the eddy current characteristics in MRI systems. In this work, we implemented a numerical approach to simulate the eddy current responses in an open compact 0.3 T MRI system that was developed for skeletal age assessment in children [15], as shown in Fig. 1.

In open MRI system, the gradient coil is of the planar type consisting of an upper and a lower coil positioned in the gap between the magnet poles (as is shown in Fig. 2). In addition, the eddy current conducting structures can have different geometric shapes, and for this reason, we searched for a more efficient process. The coupled circuit method works by subdividing each conducting structure into infinitely thin sublayers and further dividing each sublayer into subdomains. The subdomains are considered to be inductively coupled to each other and to the gradient coils also. System of first order differential equations is formulated from these networks of resistive-inductive series circuits. Eddy current transient responses in different subdomains at different spatial locations can be easily found by solving this system of first order differential equations.

Let us consider the eddy current responses in a cubic RF shielding box. We can consider the upper and lower coils as a single eddy current generating source. Following the coupled circuit approach we subdivide the brass plates in the RF box into several subdomains along the thickness and length of each plate [5, 10 – 13]. For each subdomain, we assign a self-inductance, L_i, and a dc resistance, R_i. If we represent the self-inductances (L_i) and mutual inductances among subdomains by the matrix, $\mathbf{M}_{ii}$, and the inductive couplings between the gradient coil and any subdomain by the matrix, $\mathbf{M}_{is}$, then the system of coupled circuit differential equations can be expressed as [5, 12]

$$\mathbf{M}_{ii}\frac{d\mathbf{I}(t)}{dt} + \mathbf{R}_i\mathbf{I}(t) = -\mathbf{M}_{is}\frac{di_s(t)}{dt}, \text{ where}$$

$$\mathbf{M}_{ii} = \begin{pmatrix} L_1 & M_{12} & . & M_{1n} \\ M_{21} & L_2 & . & M_{2n} \\ . & . & . & . \\ M_{n1} & M_{n2} & . & L_n \end{pmatrix}; \mathbf{M}_{is} = \begin{pmatrix} M_{1s} \\ M_{2s} \\ . \\ M_{ns} \end{pmatrix}; \mathbf{R}_i = \begin{pmatrix} R_1 & 0 & . & 0 \\ 0 & R_2 & . & 0 \\ . & . & . & . \\ 0 & 0 & . & R_n \end{pmatrix};$$

in which, $L_1,\ L_2,\ \ldots\ldots, L_n$ are the self-inductances of the subdomains; M_{12}, $M_{13},\ \ldots\ldots, M_{1n}$ are the mutual inductances between the subdomains; $M_{1s},\ M_{2s},\ \ldots\ldots, M_{ns}$ are the mutual couplings between the gradient coil and the subdomains; and $R_1,\ R_2,\ \ldots\ldots, R_n$ are the resistances of the subdomains; $i_s(t)$ is the gradient coil current which is represented in our work as trapezoidal signal in the time-domain with equal ramp-up and ramp-down time and constant flat-top current of duration much higher so that the eddy current signal can decay within this period. The signal representation can be expressed as

$$i_s(t) = \begin{cases} 0, & t \le t_1 \\ \dfrac{i_o(t-t_1)}{t_2-t_1}, & t_1 \le t \le t_2 \\ 1, & t_2 \le t \le t_3 \\ \dfrac{i_o(t_3-t)}{t_4-t_3}, & t_3 \le t \le t_4 \\ 0, & t_4 \le t \end{cases}$$

where i_o is the maximum current and parameter t_1, t_4 define the start and end point of the trapezoidal signal and, t_2, t_3 locate the shoulders of the signal. **I**(t) is the eddy current matrix with dimensions equal to the number of subdomains considered. We have applied the Eigen matrix concepts of solving differential equations to simplify and speed up the entire calculation process.

B. Simplification by the Eigen Method

We can express the above system of ordinary differential equations as

$$\frac{d\mathbf{I}(t)}{dt} = \mathbf{A}\mathbf{I}(t) + \mathbf{B}\frac{di_s(t)}{dt},$$

where $\mathbf{A} = -\mathbf{M}_{ii}{}^{-1}\mathbf{R}_i$ and $\mathbf{B} = -\mathbf{M}_{ii}{}^{-1}\mathbf{M}_{is}$. For the constant flattop portion of the gradient signal the second term ($\frac{di_s(t)}{dt}$) of the right hand side of above equation is zero and it becomes a homogeneous system of differential equations:

$$\frac{d\mathbf{I}(t)}{dt} = \mathbf{A}\mathbf{I}(t).$$

On the other hand, for the ramp-up or ramp-down duration of the gradient signal, $\frac{di_s(t)}{dt}$ is not zero and the system of differential equations becomes a nonhomogeneous differential equation problem. We treat the homogeneous case by implementing the following decoupling solution method.

Case 1: Homogeneous

Here is the general procedure: to solve a homogeneous linear system of ordinary differential equations with constant coefficients and initial values

$$\frac{d\mathbf{I}(t)}{dt} = \mathbf{A}\mathbf{I}(t), \qquad \mathbf{I}(t_0) = \mathbf{I}_0.$$

(i) Compute the eigenvalues and eigenvectors of the coefficient matrix **A**.

(ii) Use the eigenvalues and eigenvectors of **A** to respectively construct the diagonal matrix **D** and the change of basis matrix **C**, such that

$$\mathbf{D} = \mathbf{C^{-1}AC} \quad \leftrightarrow \quad \mathbf{A} = \mathbf{CDC^{-1}}.$$

(iii) Write down the general solution of the decoupled system

$$\frac{d\mathbf{z}}{dt} = \mathbf{Dz} \quad \rightarrow \quad \mathbf{z} = \begin{bmatrix} c_1 e^{\lambda_1 t} \\ \vdots \\ c_n e^{\lambda_n t} \end{bmatrix}.$$

(iv) Determine the coefficient matrix

$$\mathbf{c} = \mathbf{C}^{-1} \begin{bmatrix} I_1(t_0) e^{-\lambda_1 t_0} \\ \vdots \\ I_n(t_0) e^{-\lambda_n t_0} \end{bmatrix}.$$

(v) The solution of the original (coupled) system will be

$$\mathbf{I}(t) = \mathbf{Cz}.$$

To find the solution to the initial value problem of the nonhomogeneous equations

$$\frac{d\mathbf{z}}{dt} = \mathbf{Dz} + \mathbf{E}(t), \qquad \mathbf{I}(t_0) = \mathbf{I}_0,$$

where $\mathbf{E}(t) = \mathbf{C}^{-1}\mathbf{B}\frac{di_s(t)}{dt}$, we implement the fundamental matrix method.

Case 2: Nonhomogeneous

The general procedure is given below.

(i) The fundamental matrix was expressed as

$$\mathbf{\Phi}(t) = \begin{bmatrix} \boldsymbol{v}_{11} e^{\lambda_1 t} & \boldsymbol{v}_{12} e^{\lambda_2 t} & \ldots . \boldsymbol{v}_{1n} e^{\lambda_n t} \\ \vdots & \vdots & \vdots \\ \boldsymbol{v}_{n1} e^{\lambda_1 t} & \boldsymbol{v}_{n2} e^{\lambda_2 t} & \ldots . \boldsymbol{v}_{nn} e^{\lambda_n t} \end{bmatrix},$$

where $\boldsymbol{v}_{n1}$, $\boldsymbol{v}_{n2}$, …., $\boldsymbol{v}_{nn}$ are the associated eigenvectors, and λ_1, λ_2, …., λ_n are the eigenvalues of the corresponding homogeneous equation.

(ii) The solutions of the nonhomogeneous equations can be given by

$$\boldsymbol{I}(t) = \mathbf{\Phi}(t)\mathbf{\Phi}(0)^{-1}\mathbf{I}(t_0) + \int_{t_0}^{t} \mathbf{\Phi}(t)\mathbf{\Phi}(s)^{-1}\,\mathbf{E}(s)ds.$$

C. Coupled Circuit Modeling

To consider the skin effect of eddy current, at first, each conducting structure is subdivided into a number of ideally infinitely thin sublayers so that enough sublayers are considered to represent the skin depth more accurately [10]. For practical numerical calculation purposes, a sufficient number of sublayers is considered, so that the eddy currents in each layer can be assumed as constant. But considering a finite number of sublayers would necessarily introduce some errors in the simulation results that decrease with decreasing sublayer thickness [13]. Following the approach in references [6, 10], we have considered the thickness to be less than one-tenth of the skin depth, δ. For high frequency and/or high conductivity, the formula we took for δ can be expressed [27] as

$$\delta = \sqrt{\frac{2}{\mu\omega\sigma}},$$

where μ is the permeability, ω is the angular frequency, and σ is the conductivity. Each sublayer is again divided into several subdomains along the length or width. Because the current in each subdomain is considered to be constant, we have assumed dc resistance for each subdomain. The resistance of each subdomain is then calculated by

$$R = \rho \frac{l}{\mathrm{w}d},$$

where ρ is the resistivity and l, w, and d are the length, width, and thickness of each subdomain, respectively. The self- and mutual inductances among the subdomains are computed by applying the simple formulas (source: Ref. [28]) given in the Appendix A.

The Z-gradient coil has a combination of circular current loops wound onto a surface of fiber-reinforced plastic (FRP) plate with the diameter optimized using a genetic algorithm [15]. To calculate the inductive coupling between the planar coils (upper and lower coils) and any subdomain, we implemented the solid angle form of Ampere's law, according to which the magnetic flux density (B) is proportional to the gradient of the solid angle (Ω) subtended by an arbitrary loop carrying a current, i_{coil} [22]:

$$\mathrm{B} = \frac{-\mu_o i_{coil} \nabla \Omega}{4\pi}.$$

Here, ∇ is the gradient operator. In order to calculate the flux linkage of the gradient coil to subdomains at any position we need to formulate the solid angle expression considering any location in the three dimensional space. In our analysis, we have formulated the solid angle expression in Cartesian coordinate considering all three axes, X, Y, and Z for both Gz and Gx type coil loops by following the works done in References [17, 19 - 21]. Because of cylindrical symmetry we have followed a simple analytical solid angle calculation approach for Gz coil (circular current loop) by following the methods given in references [17, 19, and 20]. But in case of Gx coil the current loops are in asymmetric position with respect to the magnet center. To consider this fact, we have applied a simple rectangular segmentation approach to calculate the solid angle of Gx coil at any position in the region of interest (ROI) by following the method given in reference [21]. Details of the calculation methods are explained in Appendix B and Appendix C for Gz coil and Gx coil loops, respectively. A schematic diagram of the solid angle approach in coupled circuit method has been presented in Fig. 3 for a circular loop and subdomains of a conducting plate of the RF shielding box. The eddy current conducting structure is divided into sublayers and subdomains along thickness (along Z-axis) and length or width (along Y- or X-axis), respectively, so that the thickness *d* is much smaller than the skin depth of the corresponding signal frequency. If B_{dom} is the average magnetic flux density in each subdomain generated by all the current loops in the gradient set carrying an equal current i_{coil}, then the total flux across each subdomain of area A_{dom} and, hence, the inductive coupling between the gradient coil and each subdomain (M_{is}) [29] can be calculated by

$$M_{is} = {}^{\mathrm{B}_{dom} A_{dom}}/_{i_{coil}}.$$

As for the planar Z-gradient coil, it has two sets of similar coils near the magnet poles (as shown in Fig. 2). Since current circulations in these two layers of coils are opposite in

direction [14] the solid angle in the region of interest (ROI) will be of opposite sign – for anti-clockwise current circulation the solid angle is positive and for clockwise circulation it is negative [22]. If M_{ir} is the flux linkage between the *r*-th coil loop and *i*-th subdomain, then the total flux linkage to that subdomain from *n* number of loops will be

$$\sum_{r=1}^{r=n} M_{ir}$$

At any subdomain in between the magnet gap, these opposite flux linkages - induced from all of the coil loops both from the upper and the lower coil sets - are added to get total flux linkage of Gz coil to that subdomain. In this way, inductive coupling between Z-gradient coil and all of the subdomains are calculated.

In case of X-gradient coil, it also has upper and lower layer coils near the magnet poles. In addition, in each layer there have two sets of the similar coil patterns with clockwise and anti-clockwise current circulations [14]. Flux linkages of Gx coil to any subdomain in the magnet gap should consider contribution of flux linkages from these four sets of coil loops. The sign of the solid angles are considered according to the current circulation directions mentioned above. Once we have calculated all the matrices of inductances and resistances (M_{ii}, M_{is}, and R_{ii}) for a network of coupled eddy current conducting subdomains, we can implement them in the coupled differential equations to get the transient response of eddy current in different subdomains at different locations.

D. Simulation Parameters

We considered the distribution of eddy currents in the local RF shielding box induced by both Z-gradient and X-gradient coils. The shielding box was positioned within the 122 mm magnet gap, symmetrical to the center of the gradient coil. The box is made of 0.3 mm-thick brass plates of resistivity ρ, $6 \times 10^{-8}\ \Omega.\mathrm{m}$, and with boundary dimensions of 220 mm×180 mm×100 mm . Both the upper and lower Z-gradient coils have similar circular loops of maximum diameter 315.42 mm consisting of 30 circular turns. On the other hand,

the X-gradient coil were designed as a combination of circular arc and second-order Bezier curve with the position and center angle optimized using Genetic algorithm [15]. In each part there have 16 turns of coil and the coil pattern was restricted to a circular region of 320 mm in diameter. For both type of coils, each gradient coil element was made by winding polyethylene-coated copper wire of 0.6 mm diameter on a surface of fiber-reinforced plastic (FRP) plate. The applied gradient signal was of the trapezoidal type with a ramp-up and ramp-down time of 170 μs and flattop duration of 1.06 ms. The corresponding skin depth was 1.60739 mm.

Because the upper and lower plates of the local shielding box are in the X–Y plane, perpendicular to the Z-gradient (Gz) field direction, and the Z component (axial component) of the Gz field has a much higher value than the negligible X and Y components, the eddy currents can be assumed to exist mostly in the upper and lower plates of the shielding box. Following the coupled circuit method, we took two 0.15 mm-thick sublayers of each plate, which was considered to be sufficiently thin (less than one-tenth of the skin depth (1.60739 mm at 5.882 KHz)) to assume a constant eddy currents along the thickness (along the Z-axis). To consider the eddy current distribution along X- and Y- axis, we have again divided each sublayer into thin subdomains along each direction. In this simulation we have considered subdomains of equal width 2 mm. In this way, subdomains taken in each layer along X-axis was 110 and along Y-axis was 90. The number of Eigen values was twice of these values for each direction as we have divided each plate into two thin sublayers. The dimension of each subdomain divided along the length of each brass plate was 180 mm×2 mm×0.15mm and along the width was 220 mm×2 mm×0.15 mm.

E. Experimental Setup

We compared our simulation and experimental results for Z-gradient coil induced eddy current responses. The experiment was conducted using the FID measurement technique

[30]. We designed an NMR probe consisting of a solenoid RF coil wound around a 6 mm-diameter glass sphere filled with baby oil, tuning and matching capacitors, and a rectangular shield box made of brass plates. The experimental setup and the internal structure of the NMR probe are shown in Fig. 4a.

The NMR probe was located at a given position in the region of interest (ROI) by a three-axis stepper motor stage with accuracy of 0.1 *mm*, and paired FID signals with opposite gradient polarity were measured followed by a 40 μs nonselective (hard) RF pulse to calculate the temporal evolution of the eddy current fields. Experimental details with the applied gradient configuration are presented in Fig. 4b.

Results

The coupled network calculation was conducted using the Mathematica® programming platform in a desktop computer (Processor: Intel(R) Core(TM)2 Duo E7500 @ 2.93 GHz 2.93 GHz; OS: Windows 7 Professional; Memory (RAM): 4.00 GB). In the calculation, at first we performed the computation of the resistance matrix, $\mathbf{R}_i$, and the inductive coupling matrices, $\mathbf{M}_{ii}$, and $\mathbf{M}_{is}$. It took less than two minutes to compute all the matrices for Z-gradient induce eddy current responses. Then, we used these data in the network equation to compute eddy current responses. Once we had constructed these matrices for a given configuration of the MRI system, we could implement them in the calculation of eddy currents for any time-dependent current applied to the gradient coil.

A. Z-Gradient Eddy Current Response:

In our analysis, we found that the amplitudes of eddy currents along the X- or Y-axis were symmetric to the center of the plate, which is expected from the positioning of the gradient coil and the upper or lower plate of the local shielding box as illustrated in Fig. 2. Fig. 5 depicts the nature of the eddy current distribution along the X-axis of the upper plate

for the outermost sublayer. Results are given for different time instants of the decaying currents. In addition, the central subdomain was found to have the largest amplitudes.

In Fig. 6, eddy current responses are given as a function of time for few subdomains located at different positions in the X-axis direction. Fig. 6a presents the eddy current transients for several domains located on the negative X-axis and Fig. 6b is for similar domains on the positive X-axis. Here, we see that transient responses have similar characteristics on both sides from the center of the plate. We also see that the eddy current responses during both ramp-up and ramp-down have rapid transient characteristics, whereas they show a slower exponential decay when there is no change in the input gradient signal. These characteristics are found to be in agreement with the physics of a network of inductively coupled circuits. In accordance with Lenz's law, the responses of eddy currents during the rising or falling portion of the input gradient signal clearly depict the opposing nature of eddy currents in an MRI system.

The secondary magnetic fields generated by these eddy currents can be determined by the Biot–Savart law. To verify the simulation results, we conducted FID measurements of the eddy current fields. In the measurements, the NMR probe was positioned at different points in the region of interest (ROI – around the center of the magnet gap), and the same procedure was repeated. We took FID signals for two cases: a) keeping the brass box inside the magnet, and b) without the brass box. The latter case was used to measure the secondary field due to other components of the MRI system. These results were then subtracted to get the secondary field generated by eddy currents in the shielding box only.

The simulation and experimental results of transient eddy current magnetic fields are combined in Fig. 7. Results are given for several points along the Z-axis for both the positive and negative sides from the center of the region of interest (ROI). We found that similar points on either side from the axis origin (center of the magent) have nearly the same

responses with opposite polarity of field amplitudes. The time constants of the decaying transient secondary fields are listed in Fig. 8 for several points along the Z-axis. As for the experiments, each FID signal was exponentially fitted to calculate the time constants. The decaying field showed a time constant of around 170 μs. Fig. 9 depicts the results of the secondary field along the Z-axis for different instances of the gradient signal. The responses are nearly linear along the Z-axis. We found good agreement between the simulation and experimental results. Both the temporal and spatial responses in the ROI along all the three axes (X-, Y-, and Z-axis) are given in Fig. 10. Compared with the temporal–spatial response of the Z-eddy field, the secondary X- or Y-eddy field responses were found to be very small.

B. X-Gradient Eddy Current Response:

Simulation for X-gradient induced eddy currents was conducted in the similar fashion as that for the Z-gradient coil. But the solid angle for a coil in the X-gradient set is asymmetric considering the center of the magnet and also considering the center of the spherical space bounding the coil and the ROI. For this reason we have followed a segmentation solid angle calculation approach following the calculation method given in reference [21] (details are explained in Appendix C). Also Gx coil has four sets (two sets in the upper layer and two sets in the lower layer near the magnet poles) of coils compared to the two sets of coils for planar Z-gradient coil. For both of these reasons, more calculation resources were needed for the simulation of X-gradient coil generated eddy currents. The computational time become two times longer (approximately six minutes) than the time required for Z-gradient eddy current simulation. In Fig. 11 we have illustrated eddy current distribution along the X-axis. In accordance with the Gx coil response the eddy current response was found nearly zero at the center of the plate whereas subdomains considered at either side from the center show increasing values. The transient eddy current responses for few subdomains are given in Fig. 12. We have found that the Gx eddy currents decay faster

than the Gz eddy current (illustration given in Fig. 6). Fig. 13 illustrates the transient secondary magnetic fields for few points in the ROI. Compare to the Z-gradient transient eddy field (illustration given in Fig. 7), X-gradient eddy field was found to decay faster with an approximate decay time constant of 70 μs. The linear eddy current field response is given in Fig. 14. Here also we see that the secondary X-gradient fields have smaller responses than the secondary Z-gradient fields (illustration given in Fig. 9). Since the current circulates in the opposite directions in the two sets of coil in each layer of planar X-gradient coil, they also have opposing secondary magnetic field response in the region of interest (ROI).

Discussion

The flattop duration of the gradient signal we considered was long enough for the eddy currents to decay to nearly zero within this period. But for the signal with shorter flattop duration or for shorter interpulse signal sequences the eddy current might not decay to negligible value. In that case, the added effect of the remaining eddy currents before each new pulse would be required to consider in the simulation. Because of system propagation delays, the flattop duration was slightly longer than the designed signal durations. In the simulation, we considered the nominal signal durations.

In our computation of inductive coupling between the Z-gradient coil and any subdomain, we solved the analytical formula of solid angle for the circular coil patterns considering all three dimensions. The same formula can be implemented for the cylindrical Z-gradient coil with a small modification [22] in the approach to formulating the inductive coupling equation. As an example, in our study case the field variables x and y are variables and z is constant, since the upper or lower brass plates of the RF shielding box is parallel to the planar gradient coils (parallel to the X-Y plane). In case of cylindrical or ellipsoidal RF shielding box or any other conducting structures, all of the field variables (x, y, and z – which are different from the variables or parameters that define the coil geometry) would be

variable. In the calculation of magnetic flux linkage between gradient coils (Gz or Gx coil) and conducting structure of cylindrical or ellipsoidal shape we have to consider this issue and define the field variables according to the geometry of the eddy current conducting structure. The solid angle expression would remain the same as it is for the case of rectangular cubic RF shielding box.

In case of Gx coil solid angle calculation we followed a segmentation approach by dividing the area of each coil into several rectangular segments and implemented solid angle calculation formula for a rectangular section [21]. We have found this calculation approach faster in terms of computer simulation and mathematically less complex. In case of cylindrical X- or Y-gradient coil we can take the projection of the area bounded by a cylindrical loop on a plane and can easily implement the rectangular segmentation approach to formulate the analytical expression for the solid angle. Reference [31] divides the curvature of the coil into several line segments and approximates the solid angle as the angle of a polygon. This approach can also be implemented for cylindrical gradient coil solid angle calculations.

In this work, we did not simulate the secondary magnetic fields generated by eddy currents in the magnetic pole or yoke. The permeability of the ferromagnetic materials does not remain constant rather varies in accordance with the hysteresis response of the material. In the coupled circuit approach the calculation of self- and mutual inductances of the subdomains and the inductive coupling between the coil and subdomains all include permeability as a constant which is not the case for ferromagnetic materials [29]. For this reason it would be needed to model the permeability variations in the hysteresis curve [32] and formulate inductance calculations accordingly. We hope to consider this study in our future works. As the magnetic pole or yoke is much further from the ROI, the eddy currents in those components have a smaller impact on the ROI. This is clearly shown in the

experimental results in Fig. 15. In addition, there were slight variations in the magnitude of eddy current fields between simulation and experiment (see Fig. 7). In the simulation, we have not considered the coupling effect between the eddy current conducting structures. Also there might have some nonlinear eddy current responses that we plan to analyze in our future works. The stepper motor has a positioning accuracy of 0.1 *mm*, which can affect the exact positioning of the NMR probe in different positions, but we still found good similarity between our simulation and the experimental results.

In the coupled circuit approach, we found that there was no strict rule in determining the sublayer thickness, although it is generally considered that it should be as thin as possible compared with the skin depth (δ) of the corresponding signal frequency. Ideally, it should be infinitely thin. It has been suggested [13] that the thickness should be less than one-fifth of δ, whereas in Ref. [12] the thickness considered was less than one-third of the skin depth. The reason for these considerations was that the self-inductance formulas considered in these papers do not include the thickness of each subdomain. We have implemented a self-inductance formula that includes thickness to accommodate the finite thickness of each subdomain. We found that a change in thickness has a certain effect on the transient response of eddy current—amplitudes and time constants show a slight variation for different thicknesses. To consider the skin effect more rigorously, we considered the thickness of each sublayer to be less than one-tenth of the skin depth, and found our simulation results to be in good agreement with the experimental results.

Conclusion

We performed eddy current simulation of an open MRI system by implementing new approaches to the coupled circuit numerical analysis method. Eigen matrix techniques for solving matrices of differential equations were implemented to speed up the calculation. Solid angle approach was implemented in the calculation of the coupling relations between

the gradient coils and any other eddy current conducting structures that induce eddy currents. We also conducted FID measurements of eddy fields and compared these results with the simulation results. A good agreement was found between the simulation and the experiment. Our approach is fast and efficient, and can be implemented to analyze eddy currents for any MRI system. Although the effect of secondary fields due to eddy currents in the local shielding box was larger than the fields due to eddy currents in other components, in future work we intend to calculate these fields as well.

Appendix

A. Self- and Mutual Inductances of Subdomains

The self-inductance of a subdomain is given by [28, pp. 313–314]

$$\frac{\mu_0}{2\pi} l \left[Log\left(\frac{2l}{0.2235(t+a)}\right) - 1 + \frac{0.2235(t+a)}{l} \right],$$

where μ_0 is the magnetic permeability, l is the length, a is the width, and t is the thickness of each subdomain.

The mutual inductance between the subdomains was computed by the following expression [28, p. 316]:

$$\frac{\mu_0}{2\pi} l \left[Log\left(\frac{l}{d} + \sqrt{1+\frac{l^2}{d^2}}\right) - \sqrt{1+\frac{d^2}{l^2}} + \frac{d}{l} \right].$$

Here, d is the geometric mean distance between subdomains, which is equal to the distance between the centers.

B. Solid Angle Calculation for Z-gradient coil pattern

Following the work of Paxton [17] and Galiano et al. [19], we calculated the solid angle formula for the circular-type coil for three dimensions. The basic equation of solid angle formulation can be expressed as [17]

$$\Omega = \int \frac{\mathbf{n}.\mathbf{ds}}{z^2},$$

where ds is the infinitesimal area of the coil and $\mathbf{n}.\mathbf{ds}$ is the area of the projection of ds onto the plane perpendicular to z, as shown in Fig. 14. As a starting point, we took an expression derived from the equation given in [22]. The expression that describes the solid angle subtended by a circular coil of radius r at the center of a sphere is:

$$\Omega = 2\pi(1 - \cos\theta),$$

where θ represents the apex angle and $\cos\theta$ can be expressed from Fig. 14 as $\frac{\mathrm{z}}{\sqrt{z^2+r^2}}$. We can also express the above equation as

$$\Omega = 2\pi\left(1 - \frac{\mathrm{z}}{\sqrt{z^2+r^2}}\right).$$

To obtain an expression for the solid angle along the X-axis, two factors must be taken into account: first, the point at *x* is now at a distance of $\sqrt{z^2 + x^2}$ from the center of the coil, and second, from this viewpoint the coil appears to be skewed at an angle of θ_1 with respect to the normal (see the black dashed lines in Fig. 15). If we take the projection $(\cos\theta_1)$ of the skewed coil at the original position of the coil, we need to multiply $\frac{\mathrm{z}}{\sqrt{z^2+x^2}}$ with the above equation. The equation along the X-axis then becomes

$$\Omega = 2\pi\left(1 - \frac{\sqrt{z^2+x^2}}{\sqrt{z^2+x^2+r^2}}\right) \times \frac{\mathrm{z}}{\sqrt{z^2+x^2}}.$$

Now, if we skew the X-skewed coil along the Y-axis again (as shown by the red circle in Fig. 14), z will become $\sqrt{z^2 + x^2 + y^2}$ and we have to multiply the projection $(\cos\theta_2)$ of the Y-skewed coil, $\frac{\sqrt{z^2+x^2}}{\sqrt{z^2+x^2+y^2}}$, with the above equation. Therefore, the final equation can be expressed as

$$\Omega = 2\pi\left(1 - \frac{\sqrt{z^2+x^2+y^2}}{\sqrt{z^2+x^2+y^2+r^2}}\right) \times \frac{\mathrm{z}}{\sqrt{z^2+x^2}} \times \frac{\sqrt{z^2+x^2}}{\sqrt{z^2+x^2+y^2}},$$

$$or\ \ \Omega = 2\pi\left(\frac{\mathrm{z}}{\sqrt{z^2 + x^2 + y^2}} - \frac{\mathrm{z}}{\sqrt{z^2 + x^2 + y^2 + r^2}}\right).$$

C. Solid Angle Calculation for planar X- or Y-gradient coil pattern

The solid angle of Gx coil is calculated by following the research work done by H. Gotoh, et al [21] for a rectangular slit. At first we will explain in brief on the solid angle of a rectangle at a point on Z-axis. Fig. C1, shows the schematic of solid angle subtended at P (0, 0, *h*) by a rectangle ABCO with sides *a* and *b*. The solid angle subtended by this rectangle at the point P is represented by [21],

$$\Omega = h\int_0^a dx\int_0^b \frac{dy}{(x^2+y^2+z^2)^{\frac{3}{2}}}$$

The solution of this double integral has been given as [21],

$$\Omega = \tan^{-1}\frac{ab}{(a^2+b^2+h^2)^{\frac{1}{2}}}$$

Now to consider solid angle of a rectangle at any point, let us consider solid angle subtended at an arbitrary observation point P (x_p, y_p, z_p) by the rectangle B'EDC as (see Fig. C2). The solid angle can be calculated by

$$\Omega_{B'EDC} = \Omega_{OAED} - \Omega_{OAB'C}$$

The formula will become as:

$$\Omega_{B'EDC} = \tan^{-1}\frac{(x_1-x_p)(y_2-y_p)}{z_p\left[(x_1-x_p)^2+(y_2-y_p)^2+z_p\right]^{\frac{1}{2}}} - \tan^{-1}\frac{(x_1-x_p)(y_1-y_p)}{z_p\left[(x_1-x_p)^2+(y_1-y_p)^2+z_p\right]^{\frac{1}{2}}}$$

Now, we can consider the portion of a Gy coil (we have considered Gy coil pattern as its position would be more realizable to explain this approach) in first quadrant (arc NH'B' in Fig.

C3) as a combination of several rectangular sections. Here, solid angle of the arc B'F'N will be

$$\Omega_{B'F'NC} = (\Omega_{OEE'D} - \Omega_{OERC}) + (\Omega_{FF'GO} - \Omega_{FPDO}) + (\Omega_{OHH'I} - \Omega_{HQGO})$$

Total solid angle of the Gy coil (arc MNB') will be double of the above equation

$$\Omega_{Total} = 2\Omega_{B'F'NC}$$

In this fashion we can divide the arc of any gradient coil into enough rectangular sections and calculate the solid angle with some approximations.

References

[1] R. M. Henkelman, M. J. Bronskill, Artifacts in magnetic resonance imaging, Rev. Magn. Reson. Med. 2 (1987) 1 – 126.

[2] D. G. Hughes, S. Robertson, P. S. Allen, Intensity artifacts in MRI caused by gradient switching in an animal-size NMR magnet, Magn. Reson. Med. 25 (1992) 167 – 179.

[3] J.J. Van Vaals, A.H. Bergman, Optimization of eddy current compensation, J. Magn. Reson. 90 (1990) 52 – 70.

[4] H. S. Lopez, F. Freschi, A. Trakic, E. Smith, J. Herbert, M. Fuentes, S. Wilson, L. Liu, M. Repetto, S. Crozier, Multilayer integral method for simulation of eddy currents in thin volumes of arbitrary geometry produced by MRI gradient coils, Magn. Reson. Med. 71, 5 (2014) 1912 – 1922.

[5] H.S. Lopez, M. Poole, S. Crozier, Eddy current simulation in thick cylinders of finite length induced by coils of arbitrary geometry, J. Magn. Reson. 207 (2010) 251 – 261.

[6] T. Weiland, Time domain electromagnetic field computation with finite difference methods, Int. J. Num. Model. : Elec. Net. Dev. Fields 9 (1996) 296 – 319.

[7] F. Liu, S. Crozier, An FDTD model for calculation of gradient-induced eddy currents in MRI system, IEEE Trans. Magn. 42 (2006) 3854 – 3860.

[8] A. Trakic, H. Wang, F. Liu, H. Sanchez-Lopez, S. Crozier, Analysis of transient eddy currents in MRI using a cylindrical FDTD method, IEEE Trans. Appl. Supercond. 16 (2006) 1924 – 1936.

[9] J. B. Schneider, Planes waves in FDTD simulations and a nearly perfect total-field/scattered field boundary, IEEE Trans. Anten. Prop. 52 (2004) 3280 – 3287.

[10] M.J. Sablik, R.E. Beissner, A. Choy, An alternative numerical approach for computing eddy currents: case of the double-layered plate, IEEE Trans. Mag. 20 (1984) 500 – 506.

[11] T. Takahashi, Numerical Analysis of eddy current problems involving z gradient coils in superconducting mri magnets, IEEE Trans. Mag. 26 (1990) 893 – 896.

[12] T.K. Kidane, W.A. Edelstein, T.P. Eagan, V. Taracila, T.N. Baig, Y.-C.N. Cheng, R.W. Brown, Active-passive shielding for mri acoustic noise reduction: network analysis, IEEE Trans. Mag. 42 (2006) 3854 – 3860.

[13] M. Poole, H.S. Lopez, O. Ozaki, H. Kitaguchi, I. Nakajima, S. Urayama, K. Sato, H. Fukuyama, S. Crozier, Simulation of gradient coil induced eddy currents and their effects in a head-only HTS MRI magnet, IEEE Trans. App. Super. 21 (2011) 3592 – 3598.

[14] Jianming Jin, *Analysis and design in magnetic resonance imaging*, CRC Press, 1999.

[15] Y. Terada, S. Kono, D. Tamada, T. Uchiumi, K. Kose, R. Miyagi, E. Yamabe, H. Yoshioka, Skeletal age assessment in children using an open compact mri system, Magn. Reson. Med. 69 (2013) 1697 – 1702.

[16] S. Handa, T. Haishi, K. Kose, Development of a local electromagnetic shielding for an extremity magnetic resonance imaging system, Rev. Sci. Ins. 79 (2008) 113706-1 – 3.

[17] F. Paxton, Solid Angle Calculation for a Circular Disk, Rev. Sci. Inst. 30 (1959) 254 – 258.

[18] H. M. Haitjema, Evaluating solid angles using contour integrals, Appl. Math. Mod. 11 (1987) 69 – 71.

[19] E. Galiano, C. Pagnutti, An analytical solution for the solid angle subtended by a circular detector for a symmetrically positioned linear source, Appl. Rad. Isot. 64 (2006) 603 – 607.

[20] S. Pomme, L. Johansson, G. Sibbens, B. Denecke, An algorithm for the solid angle calculation applied in alpha-particle counting, Nucl. Inst. Meth. Phys. Res. A 505 (2003) 286 – 289.

[21] H. Gotoh, H. Yagi, Solid angle subtended by a rectangular slit, Nucl. Inst. Meth. 96 (1971) 485 – 486.

[22] W.T. Scott, *The physics of electricity and magnetism*, 2nd Edition, John Wiley& Sons, Inc., Tokyo, 1959.

[23] P. Jehenson, M. Westphal, N. Schuff, Analytical method for the compensation of eddy current-effects by pulsed magnetic field gradients in nmr systems, J. Magn. Reson. 90 (1990) 264 – 278.

[24] Q. Liu, D. G. Hughes, P. S. Allen, Quantitative characterization of the eddy current fields in a 40-cm bore superconducting magnet, Magn. Reson. Med. 31 (1994) 73 – 76.

[25] C. P. Bean, R. W. DeBlois, L. B. NesBitt, Eddy-current method for measuring the resistivity of metals, J. Appl. Phy. 30 (1959) 1976 – 1980.

[26] J. LePage, A. Bernalte, D. A. Lindholm, Analysis of resistivity measurements by the eddy current decay method, Rev. Sci. Intrs. 39 (1968), 1019 – 1026.

[27] J. D. Jackson, *Classical electrodynamics*, 3rd edition, New York: Wiley, 1998.

[28] E. B. Rosa, *The self and mutual inductances of linear conductors*, National Bureau of Standards, Vol. 4, (1908), 301 – 344.

[29] R. Plonsey, R.E. Collin, *Principles and applications of electromagnetic fields*, McGraw-Hill Book Company, Inc., 1961, page 274.

[30] M.A. Bernstein, K.F. King, X.J. Zhou, *Handbook of MRI pulse sequences*, Elsevier Academic Press, 2004.

[31] R. P. Gardner, K. Verghese, On the solid angle subtended by a circular disc, Nucl. Inst. Meth. 93 (1971) 163 – 167.

[32] A. Visintin, On the Preisach model of hysteresis, Non. Anal. Theory, Meth. Appl. 8 (9) (1984) 966 – 977.

Fig. Captions

Fig. 1. Open compact 0.3 T magnetic resonance imaging (MRI) system for skeletal age assessment in children.

Fig. 2. Schematic representation of the open compact MRI system. The planar gradient coil consisted of an upper and a lower coil, shown separately on the right side of the diagram. The local RF shielding box is positioned in between these coils. Eddy currents are expected to be created in the brass plates of the boundary of the RF box, and the secondary magnetic fields created by these eddy currents have a major effect on the region of interest (ROI) .

Fig. 3. A schematic representation of the solid angle approach implemented in the coupled circuit numerical method is shown for a circular turn of coil. Imaginary slices are considered as inductively coupled subdomains of minimal thickness.

Fig. 4. Experimental setup to conduct FID measurements of eddy current fields. (a) The NMR probe was positioned at a given position by a three-axis stepper motor stage with accuracy of 0.1 mm. The NMR probe consisted of a solenoid RF coil wound around a 6 mm-diameter glass sphere filled with baby oil, tuning and matching capacitors, and a rectangular shield box made of brass plates. (b) Schematics of the signaling in the FID experiment. An amplitude of 5 A of the trapezoidal signal with a nominal rise and fall time of 170 μs and constant duration of 1.06 ms was used in the experiment. An RF hard pulse was applied immediately after the gradient and FID signals were measured for the opposite gradient polarity signals by the NMR probe.

Fig. 5. Eddy current amplitudes along (a) the X-axis in the upper plate of the RF shielding box. The plate was subdivided into sublayers along the thickness (along the Z-axis). Here, results are given for the outermost layer. A symmetric current distribution from the center of the plate is seen in the diagram.

Fig. 6. Transient response of eddy currents for subdomains taken at different points (a) along the negative X-axis and (b) along the positive X-axis with respect to the center of the magnet. The brass plates are divided along the X-axis into 110 subdomains of width 2 mm each. Distances along the X-axis (that are mentioned in the diagrams) are measured by multiplying the number of the subdomains and the width of each subdomain. Responses are given for the applied gradient signal of trapezoidal shape with rise and fall times of 170 μs and a plateau length of 1.06 ms. Eddy currents are found to be opposing the changes in the gradient coil signal, thus reducing the amplitudes and delaying the signal responses of the original gradient current. Also, we see a symmetric response for subdomains at the same distance from the center of the plate.

Fig. 7. The transient responses of secondary magnetic fields generated in the ROI by the eddy currents in the local shielding box. Responses are given for (a) simulation and (b) experiment for several points on both the positive and negative sides along the Z-axis. The total signal duration was 1.4 ms and secondary responses were given from 1.6 ms. The measurements were conducted for the conditions of the brass box in the ROI and without the brass box. The eddy field without the brass box was measured to account for the effect of eddy currents other than those in the brass box. These fields were subtracted to find the eddy fields due to eddy currents in the brass box only. The simulation results were in good agreement with the experimental results.

Fig. 8. The experimental and simulated time constants for several points on the Z-axis within the ROI.

Fig. 9. Linear eddy field responses for three different time instants calculated after the end of the applied gradient current. Good agreement was found between (a) simulation and (b) experimental results.

Fig. 10. Secondary transient magnetic fields along the (a) Z-axis, (b) X-axis and, (c) Y-axis in the ROI as a result of Z-gradient-induced eddy currents in the RF shielding box.

Fig. 11. Eddy current distribution along the X-axis induced by X-gradient coil. In accordance with the field response of the X-gradient coil, the distributed eddy currents were found to be nearly zero at the center of the brass plate and increasing or decreasing values on opposite sides from the center.

Fig. 12. Eddy current transient response induced by X-gradient coil. Here responses are given for few subdomains located at different position on the X-axis.

Fig. 13. The X-gradient coil generated eddy current field is illustrated here for few points along the X-axis. X-gradient generated eddy field decays faster than the Z-gradient induced secondary magnetic field.

Fig. 14. Linear secondary magnetic field induced by X-gradient coil.

Fig. 15. Eddy current fields as a result of eddy currents induced in components of the MRI system other than the local RF shielding box.

Fig. B1. Geometric representation of the solid angle of a circular coil. Here, θ is the apex angle of the solid angle subtended at a distance r_0 by a circular coil of radius *r*.

Fig. B2. Geometric representation of a solid angle calculation in the X–Y plane. The dotted schematics represent the inclinations of the coil to account for the projection of the solid angle considering any point in the X–Y plane. θ_1 and θ_2 are the projection angles for any point along the X- and Y- axis, respectively, and ab and bc are the distances from the center along the X- and Y- axis, respectively.

Fig. C1. Geometry for the calculation of solid angle subtended by a rectangular section ABCO at a distance *h* on the Z-axis.

Fig. C2. Geometry for the calculation of solid angle subtended by an arbitrary rectangle at any field point P (x_p, y_p, z_p).

Fig. C3. Rectangular segmentation approach in the calculation of solid angle subtended by the X- or Y-gradient coil. Here half of the area of a coil is divided into several rectangular sections. The total solid angle would be twice of the solid angle subtended by this portion in first quadrant.

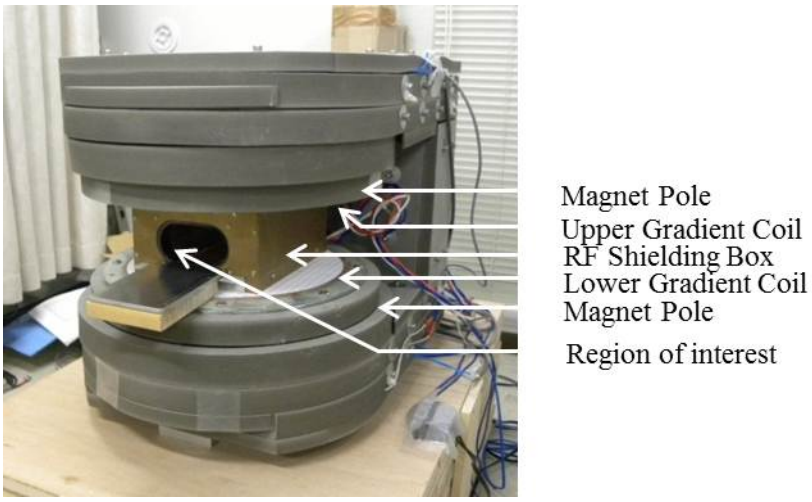
Magnet Pole
Upper Gradient Coil
RF Shielding Box
Lower Gradient Coil
Magnet Pole
Region of interest

Fig. 1

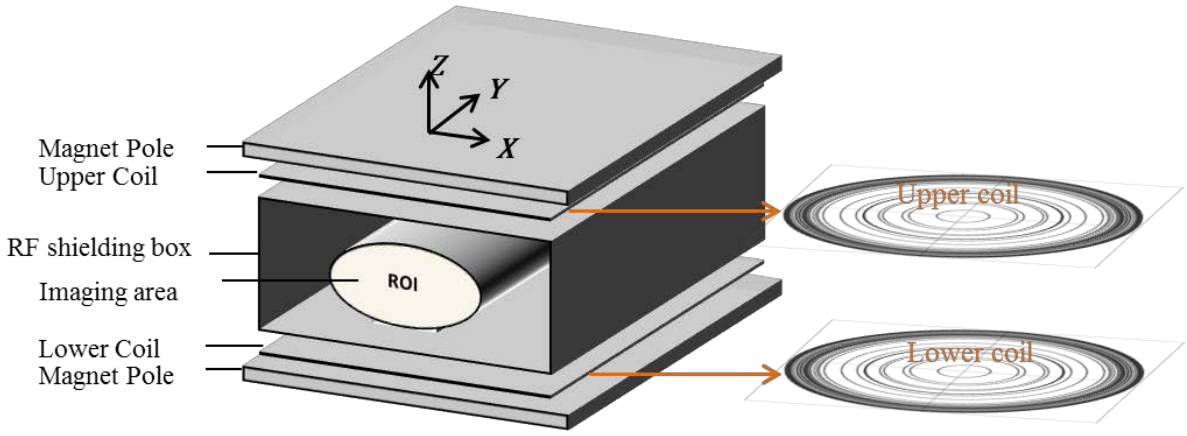
Z
Y
X
Magnet Pole
Upper Coil
RF shielding box
Imaging area
Lower Coil
Magnet Pole
ROI
Upper coil
Lower coil

Fig. 2

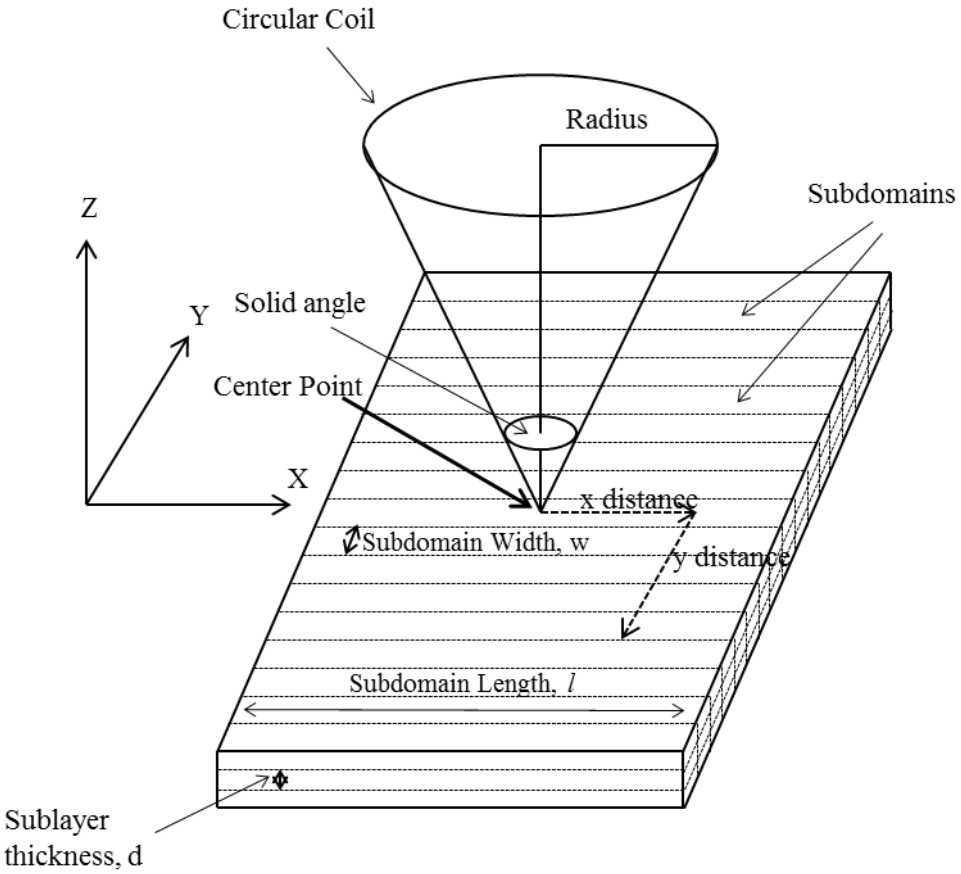
Circular Coil
Radius
Subdomains
Z
Y
Solid angle
Center Point
X
x distance
Subdomain Width, w
y distance
Subdomain Length, l
Sublayer
thickness, d

Fig. 3

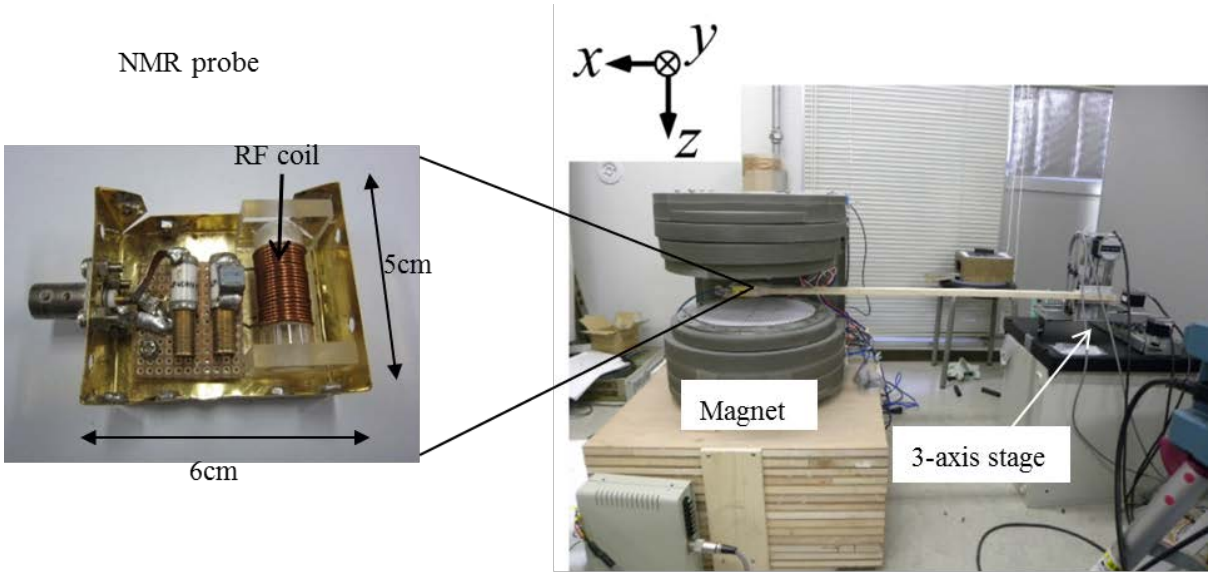
NMR probe
RF coil
5cm
6cm
x
y
z
Magnet
3-axis stage

(a)

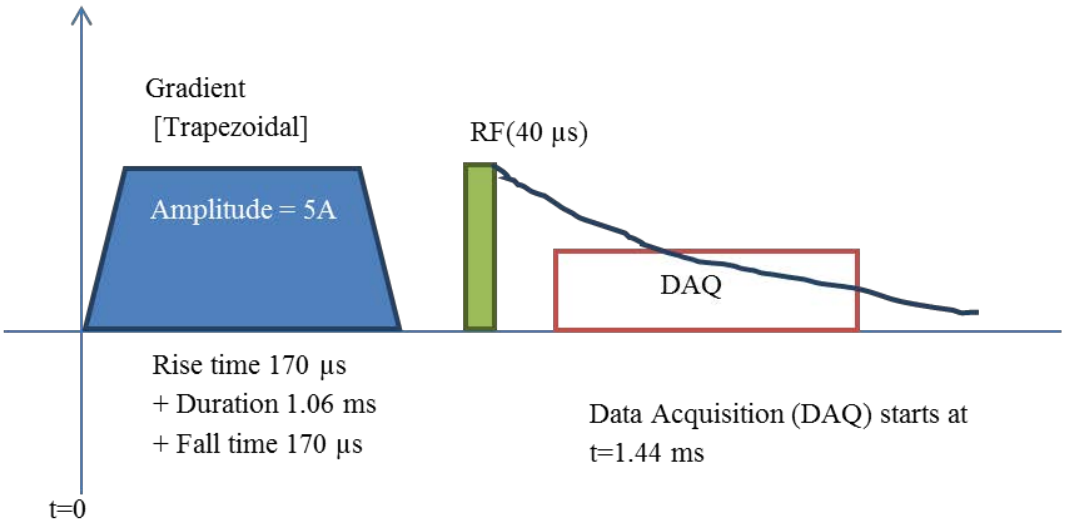
Gradient
[Trapezoidal]
Amplitude = 5A
RF(40 μs)
DAQ
Rise time 170 μs
+ Duration 1.06 ms
+ Fall time 170 μs
t=0
Data Acquisition (DAQ) starts at
t=1.44 ms

(b)

Fig. 4

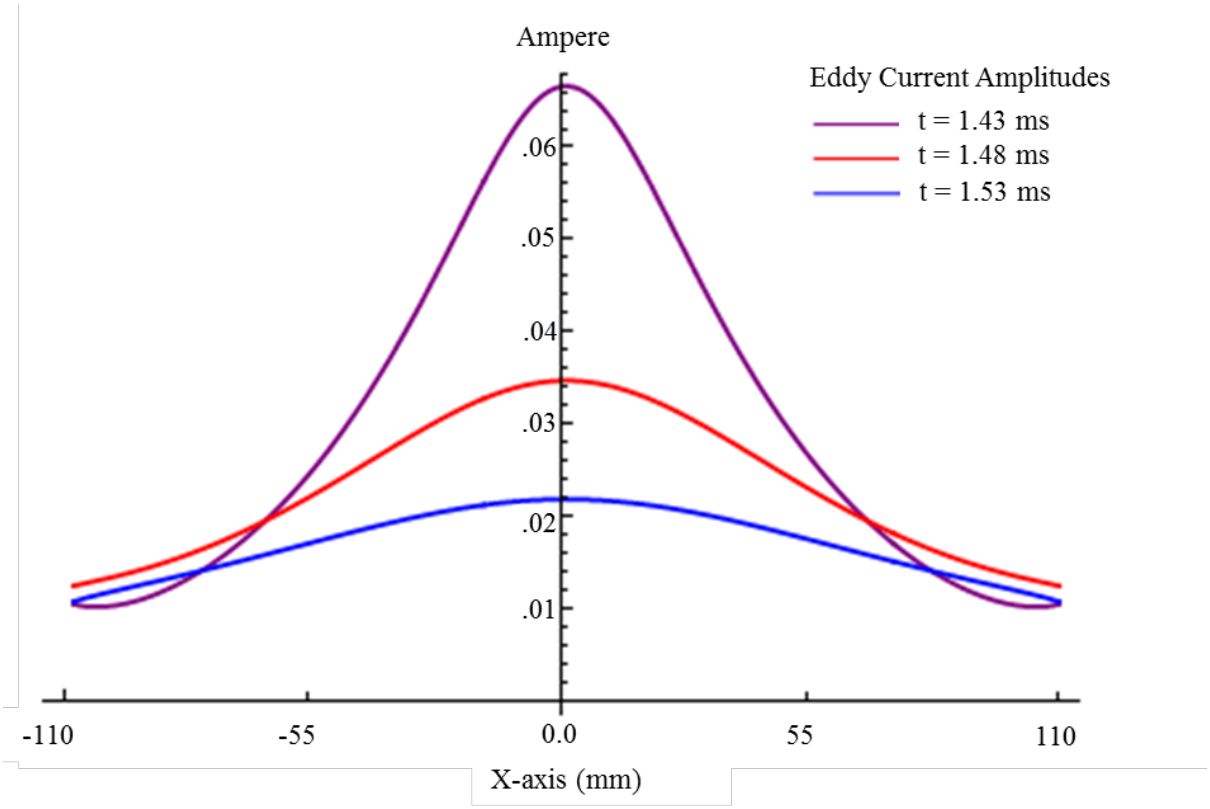
Ampere
Eddy Current Amplitudes
t = 1.43 ms
t = 1.48 ms
t = 1.53 ms
.06
.05
.04
.03
.02
.01
-110
-55
0.0
55
110
X-axis (mm)

Fig. 5

Fig. 6

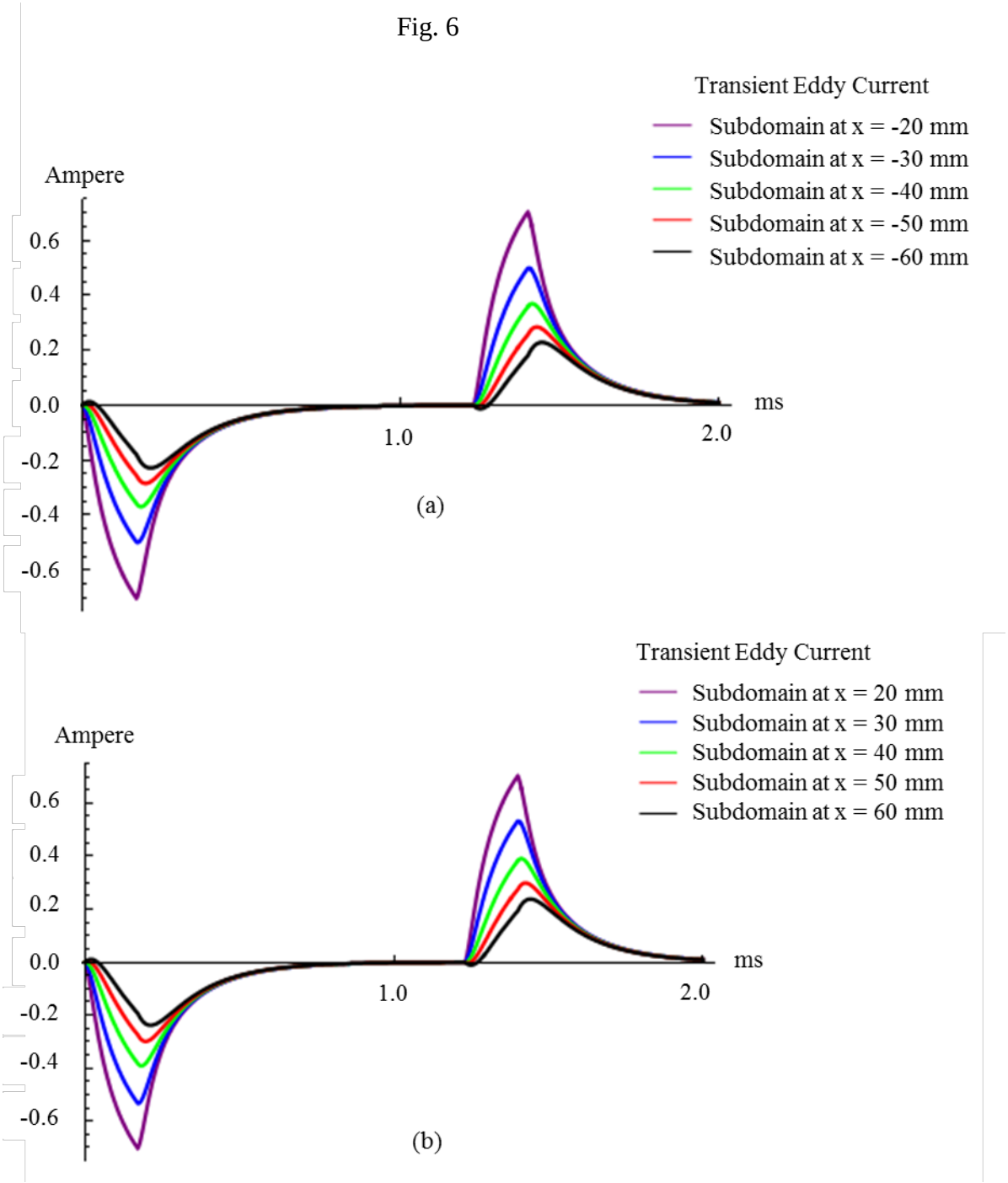
Transient Eddy Current
Subdomain at x = -20 mm
Subdomain at x = -30 mm
Subdomain at x = -40 mm
Subdomain at x = -50 mm
Subdomain at x = -60 mm
Ampere
0.6
0.4
0.2
0.0
-0.2
-0.4
-0.6
1.0
2.0
ms
(a)
Transient Eddy Current
Subdomain at x = 20 mm
Subdomain at x = 30 mm
Subdomain at x = 40 mm
Subdomain at x = 50 mm
Subdomain at x = 60 mm
Ampere
0.6
0.4
0.2
0.0
-0.2
-0.4
-0.6
1.0
2.0
ms
(b)

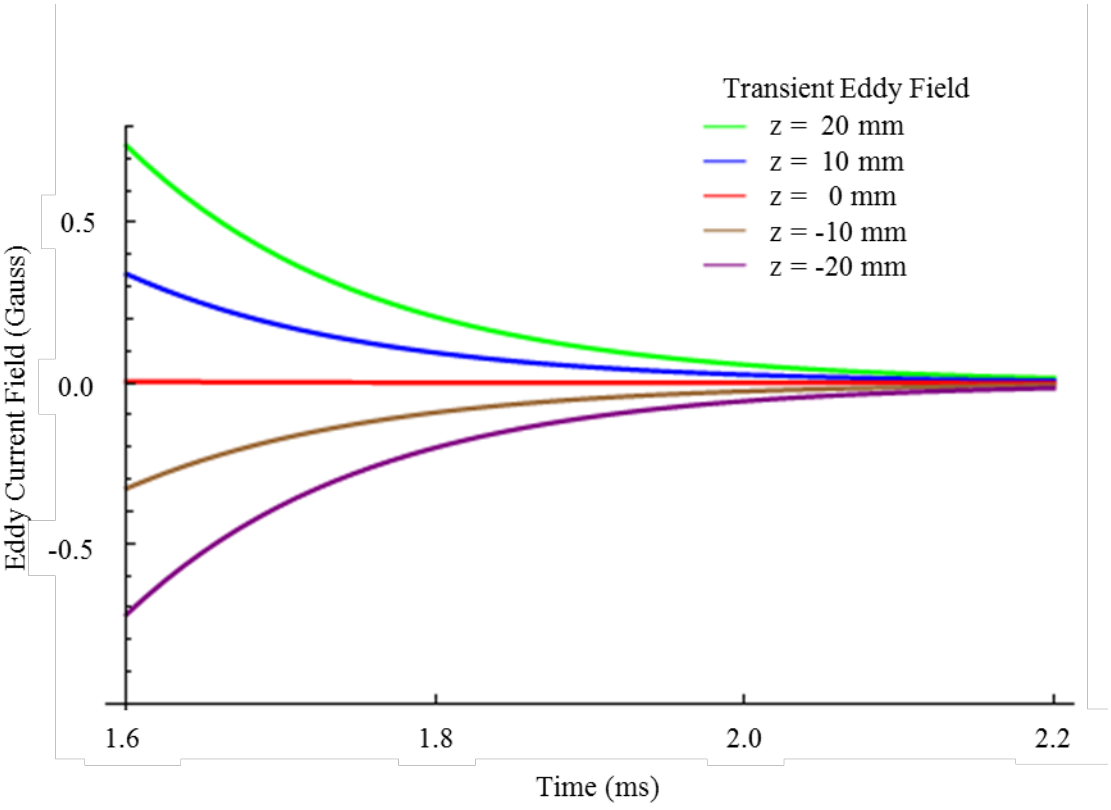
Transient Eddy Field
z = 20 mm
z = 10 mm
z = 0 mm
z = -10 mm
z = -20 mm
Eddy Current Field (Gauss)
0.5
0.0
-0.5
1.6
1.8
2.0
2.2
Time (ms)

(a)

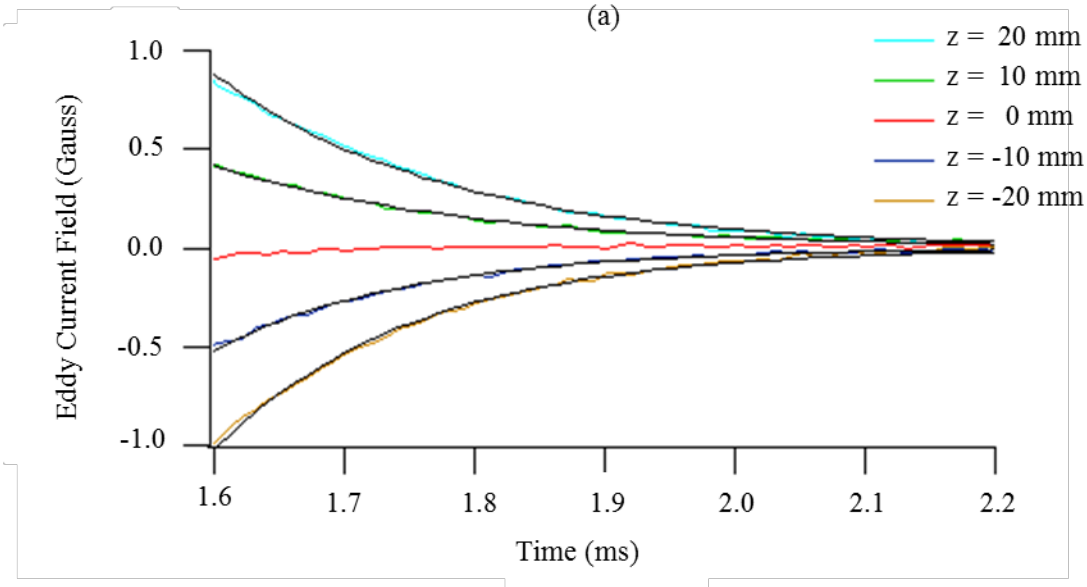
z = 20 mm
z = 10 mm
z = 0 mm
z = -10 mm
z = -20 mm
Eddy Current Field (Gauss)
1.0
0.5
0.0
-0.5
-1.0
1.6
1.7
1.8
1.9
2.0
2.1
2.2
Time (ms)

(b)

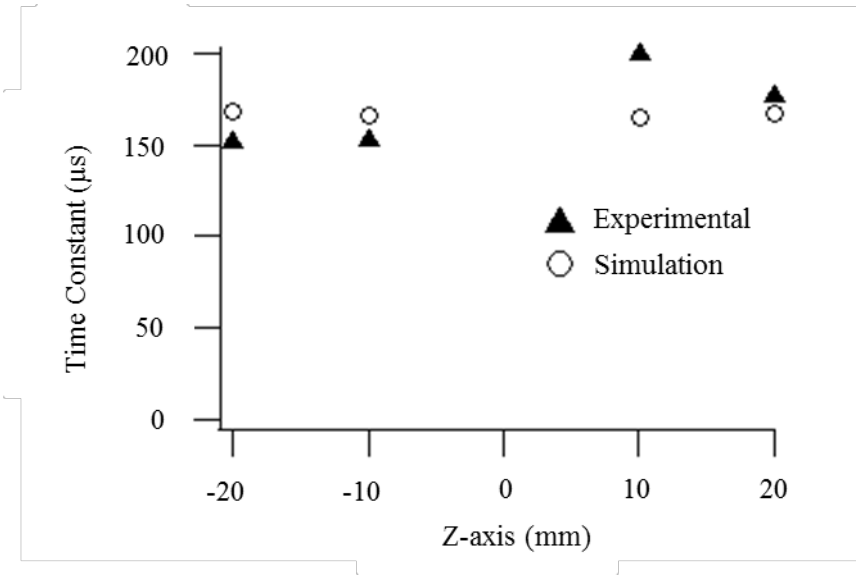
200
150
100
50
0
Time Constant (µs)
Experimental
Simulation
-20
-10
0
10
20
Z-axis (mm)

Fig. 8

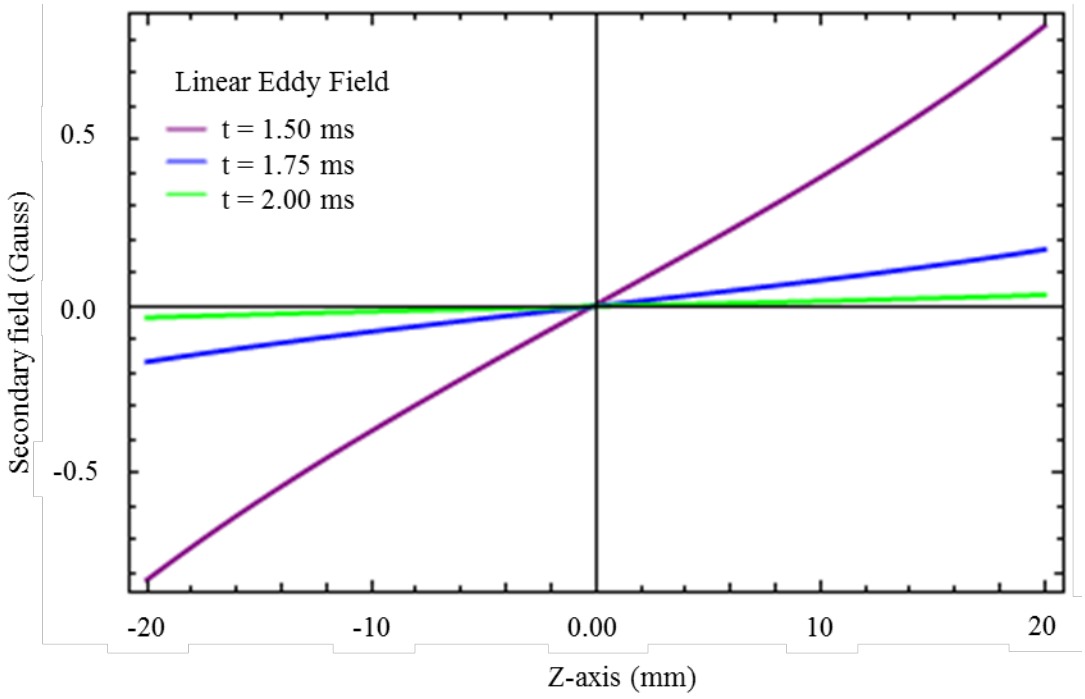
Linear Eddy Field
t = 1.50 ms
t = 1.75 ms
t = 2.00 ms
Secondary field (Gauss)
0.5
0.0
-0.5
-20
-10
0.00
10
20
Z-axis (mm)

(a)

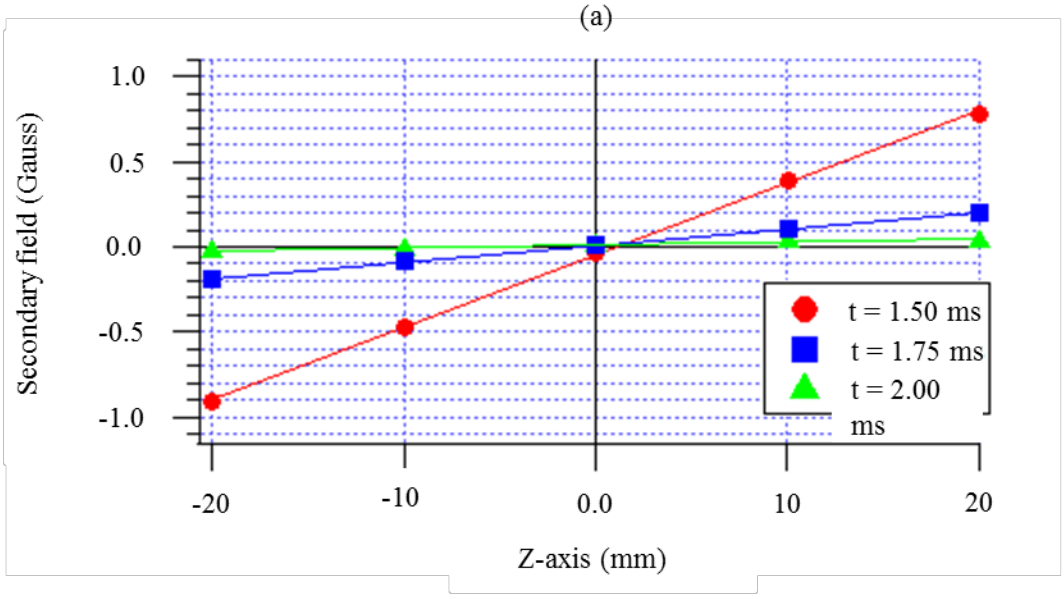
Secondary field (Gauss)
1.0
0.5
0.0
-0.5
-1.0
-20
-10
0.0
10
20
Z-axis (mm)
t = 1.50 ms
t = 1.75 ms
t = 2.00 ms

(b)

Fig. 9

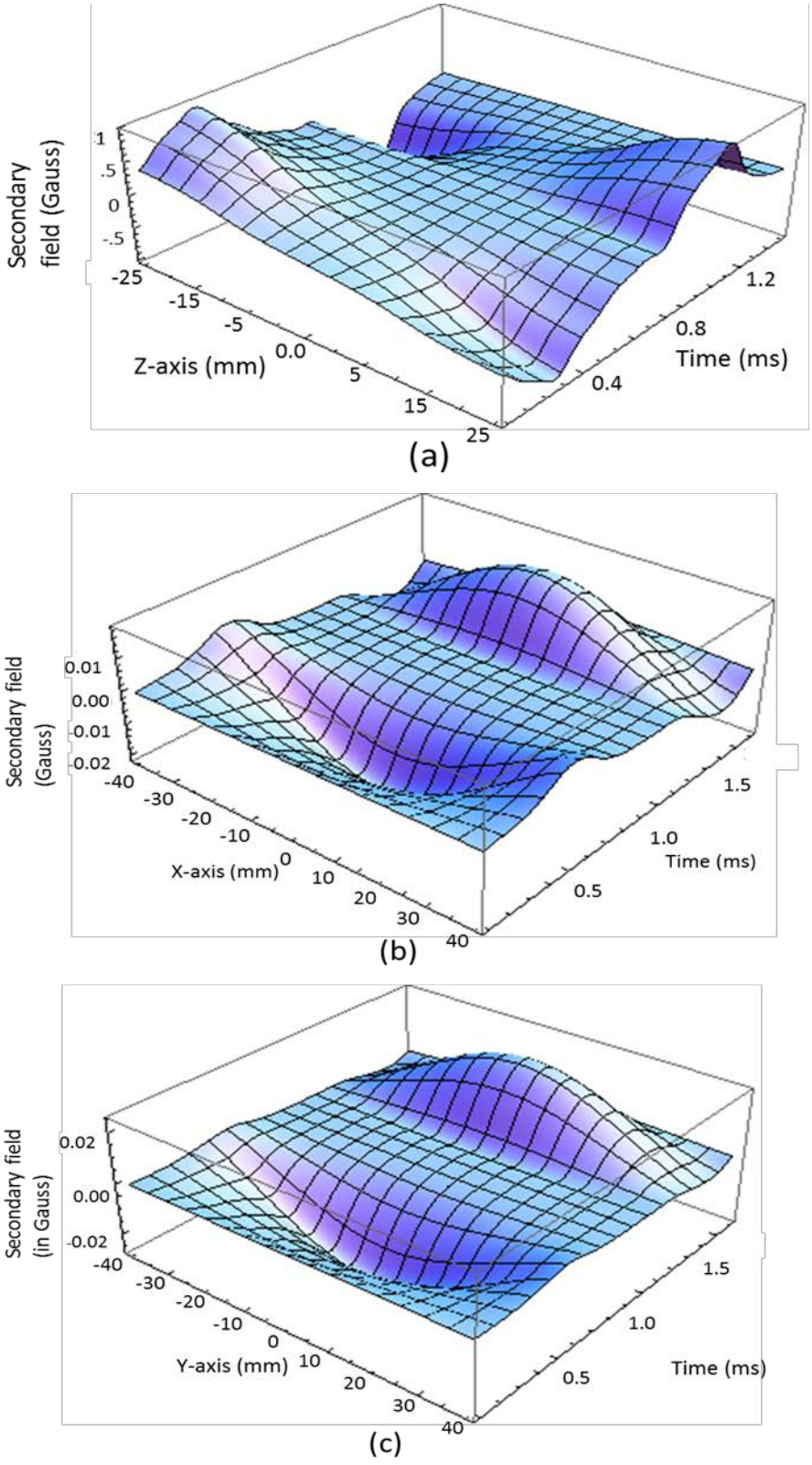
Secondary field (Gauss)
1
.5
0
-.5
-25
-15
-5
0.0
5
15
25
Z-axis (mm)
0.4
0.8
1.2
Time (ms)
(a)
Secondary field (Gauss)
0.01
0.00
0.01
0.02
-40
-30
-20
-10
0
10
20
30
40
X-axis (mm)
0.5
1.0
1.5
Time (ms)
(b)
Secondary field (in Gauss)
0.02
0.00
-0.02
-40
-30
-20
-10
0
10
20
30
40
Y-axis (mm)
0.5
1.0
1.5
Time (ms)
(c)

Fig. 10

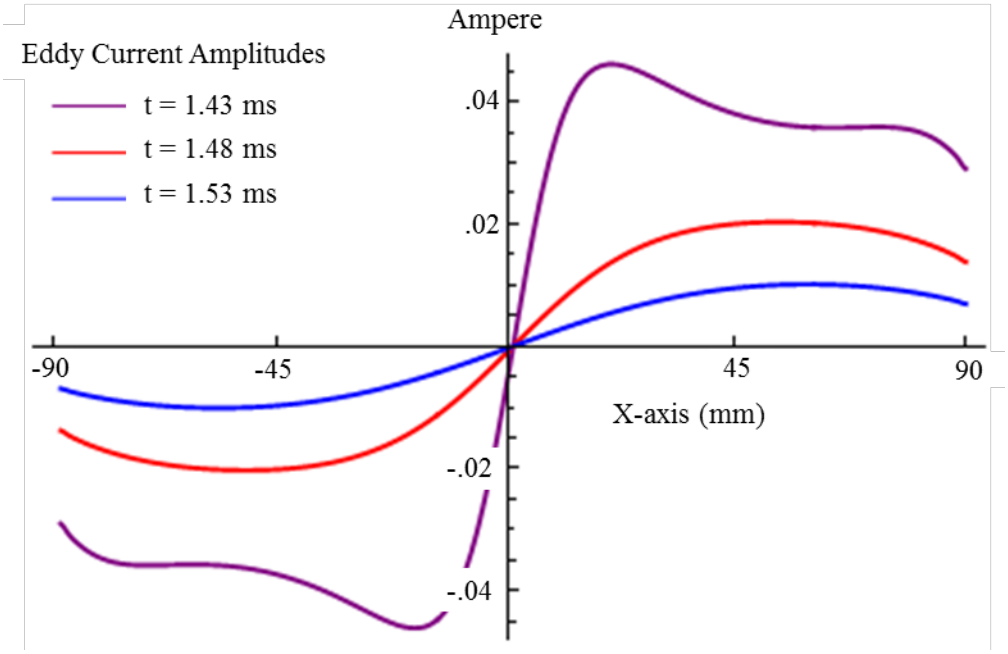
Ampere
Eddy Current Amplitudes
t = 1.43 ms
t = 1.48 ms
t = 1.53 ms
.04
.02
-.02
-.04
-90
-45
45
90
X-axis (mm)

Fig. 11

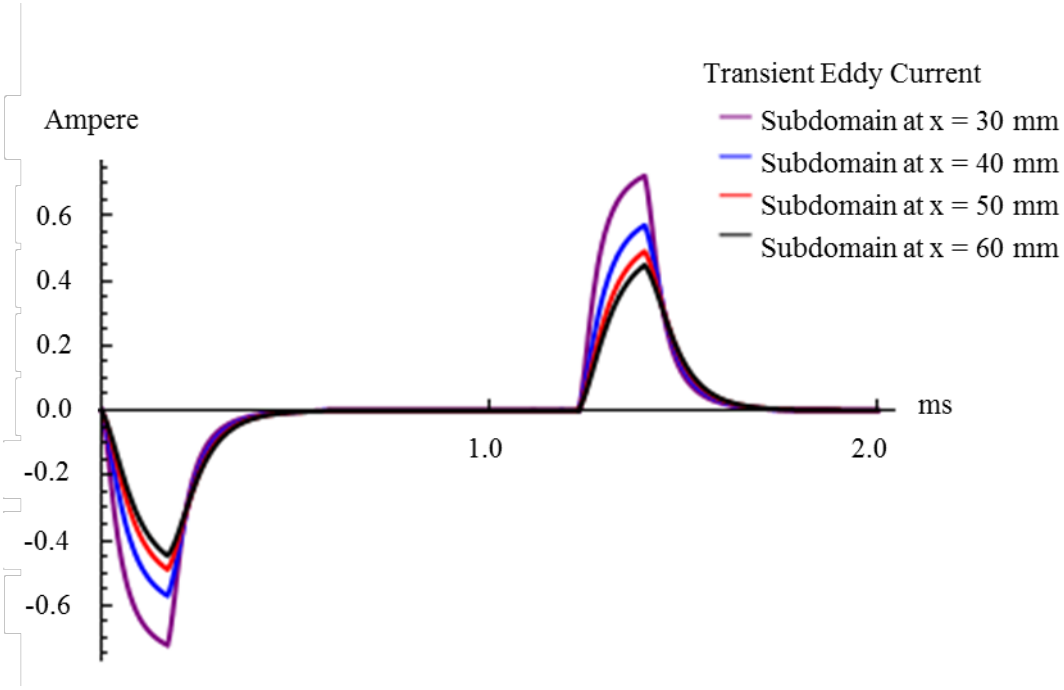
Transient Eddy Current
Subdomain at x = 30 mm
Subdomain at x = 40 mm
Subdomain at x = 50 mm
Subdomain at x = 60 mm
Ampere
0.6
0.4
0.2
0.0
-0.2
-0.4
-0.6
1.0
2.0
ms

Fig. 12

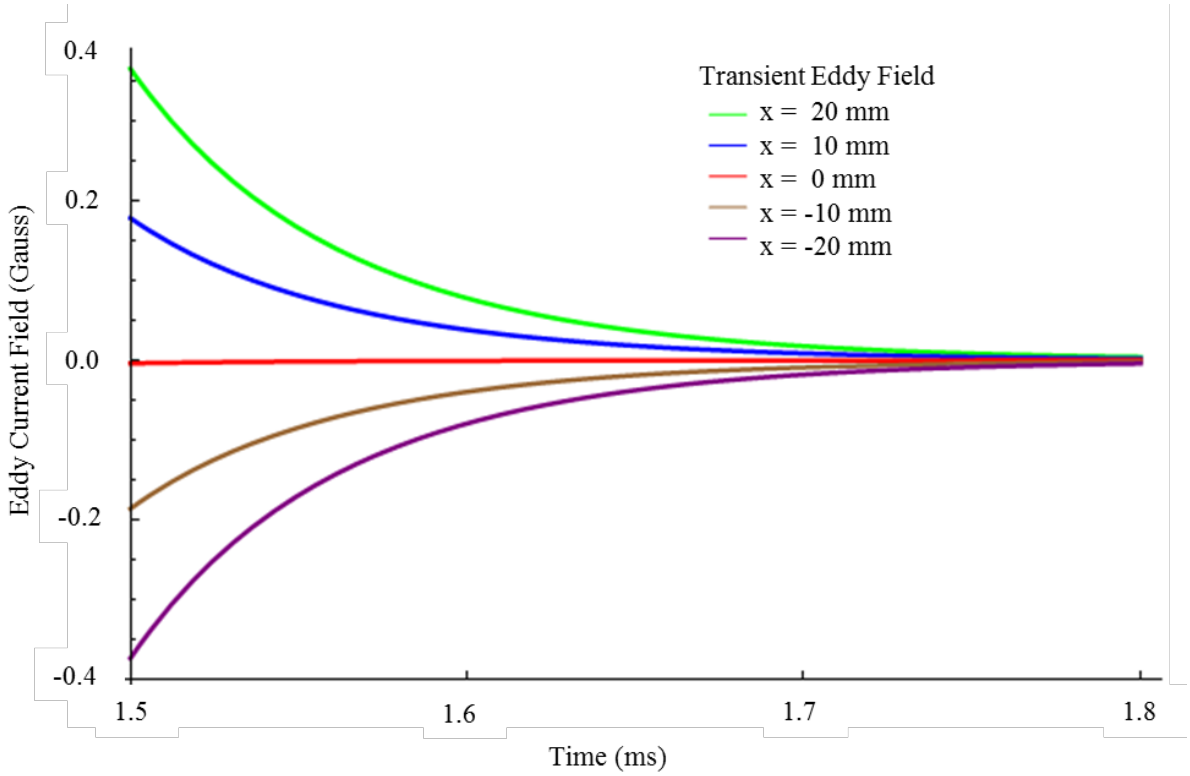
Transient Eddy Field
x = 20 mm
x = 10 mm
x = 0 mm
x = -10 mm
x = -20 mm
Eddy Current Field (Gauss)
0.4
0.2
0.0
-0.2
-0.4
1.5
1.6
1.7
1.8
Time (ms)

Fig. 13

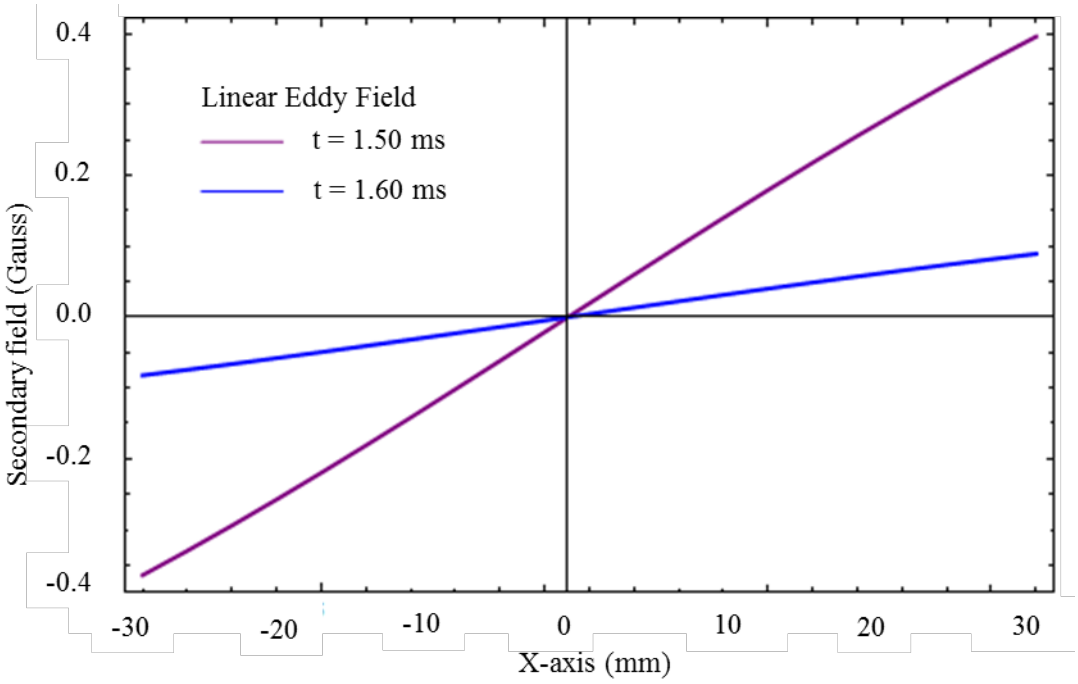
Linear Eddy Field
t = 1.50 ms
t = 1.60 ms
Secondary field (Gauss)
X-axis (mm)
0.4
0.2
0.0
-0.2
-0.4
-30
-20
-10
0
10
20
30

Fig. 14

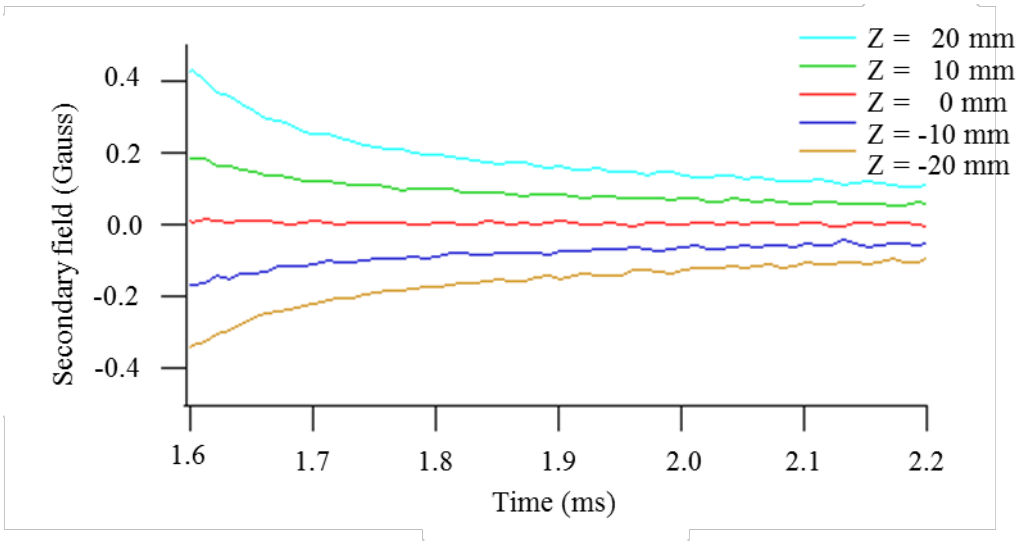
Z = 20 mm
Z = 10 mm
Z = 0 mm
Z = -10 mm
Z = -20 mm
Secondary field (Gauss)
0.4
0.2
0.0
-0.2
-0.4
1.6
1.7
1.8
1.9
2.0
2.1
2.2
Time (ms)

Fig. 15

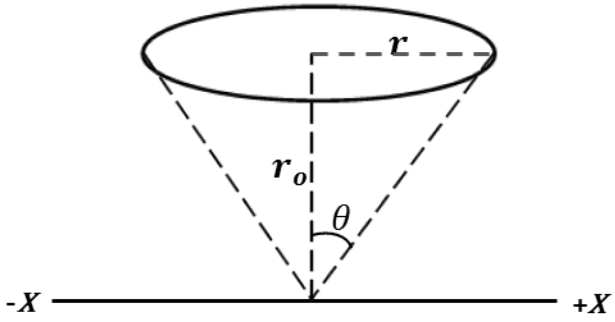

Fig. B1

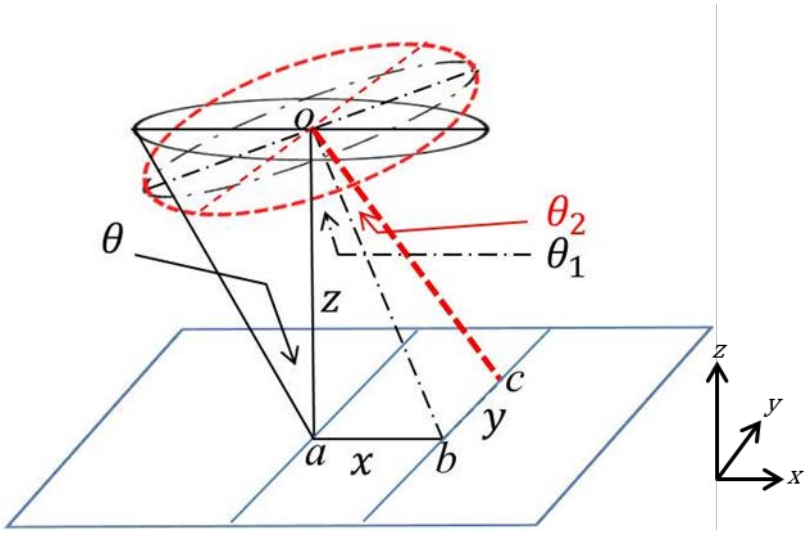

Fig. B2

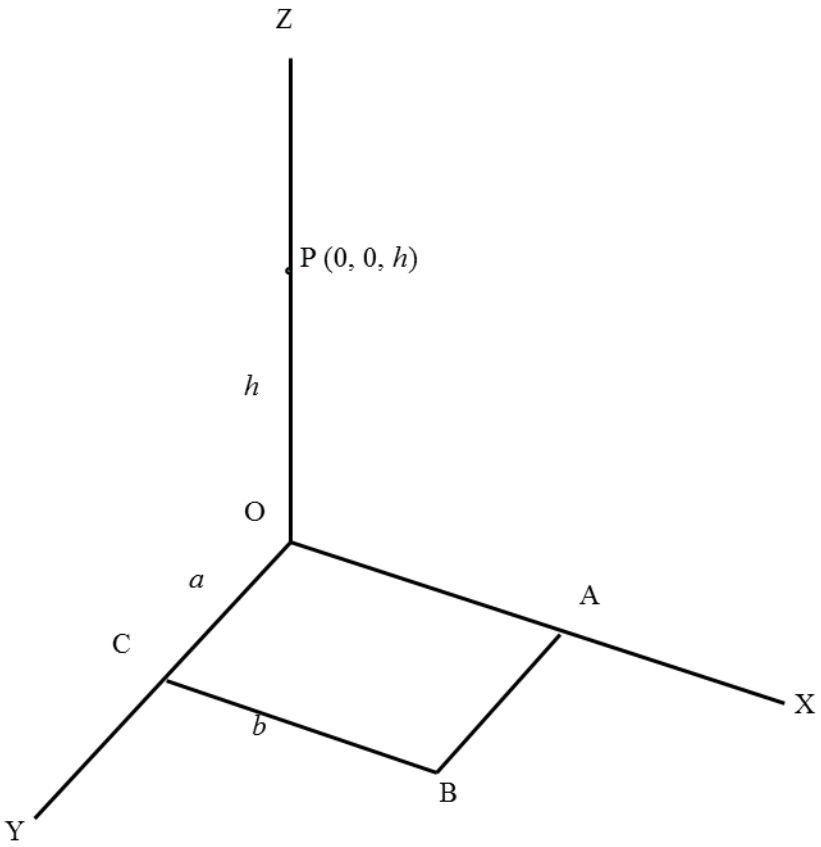

Fig. C1

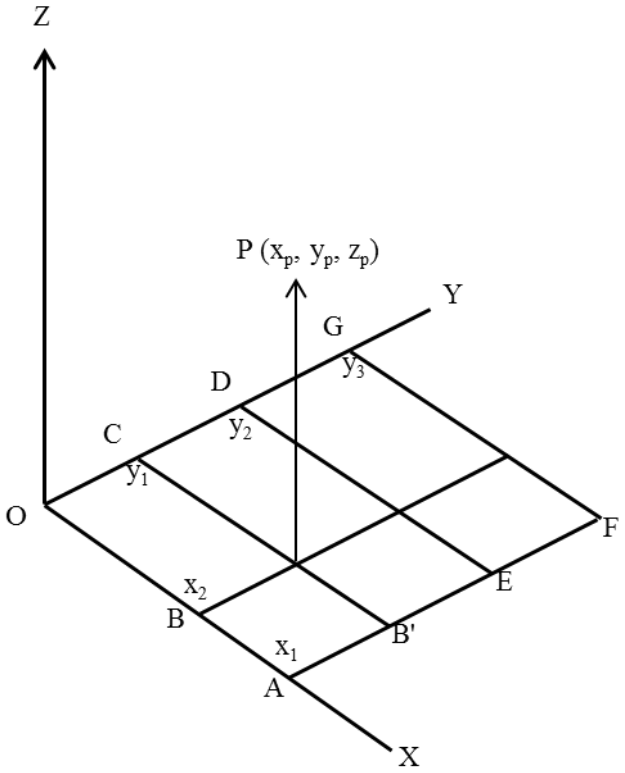

Fig. C2

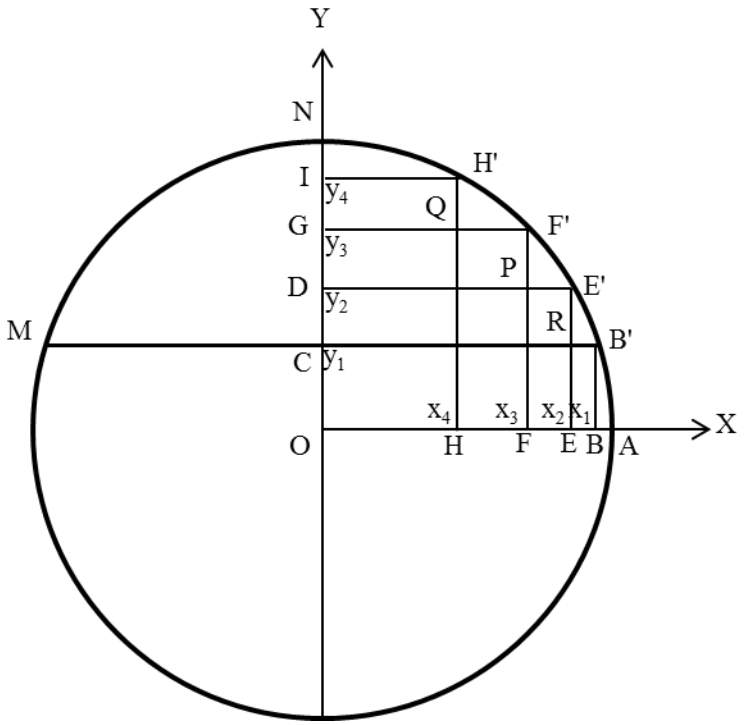

Fig. C3